ELSEVIER SERIES IN **MECHANICS OF ADVANCED MATERIALS**

PERIDYNAMIC MODELING, NUMERICAL TECHNIQUES, AND APPLICATIONS

Edited by
ERKAN OTERKUS, SELDA OTERKUS, AND ERDOGAN MADENCI

ELSEVIER

CHAPTER

12

Modeling biological materials with peridynamics

Emma Lejeune[1], *Christian Linder*[2]

[1] Department of Mechanical Engineering, Boston University, Boston, MA, United States; [2] Department of Civil and Environmental Engineering, Stanford University, Stanford, CA, United States

OUTLINE

1. Introduction 250

2. Methodology 252
2.1 Background and notation 252
2.2 Implementing growth and remodeling 256
2.3 Note on emergent behavior 258

3. Example applications 264
3.1 Fracture in biological materials 264
3.2 Tissue growth and shrinkage 264
3.2.1 Cell division and tissue growth 265
3.2.2 Cell death and tissue shrinkage 265
3.3 Connecting emergent behavior across scales 266

4. Conclusion and outlook 268

Acknowledgments 269

References 269

Peridynamic Modeling, Numerical Techniques, and Applications
https://doi.org/10.1016/B978-0-12-820069-8.00005-6

1. Introduction

From a mechanical modeling perspective, capturing the behavior of biological materials presents a compelling challenge for three main reasons. First, biologically derived materials often have a complex microstructure that can lead to mechanical response that is quite different from standard engineering materials (Meador et al., 2020). For example, shell composites such as nacre have been shown to have unprecedented fracture toughness in relation to their yield strength (Shao et al., 2012). Second, biological materials can adapt in response to their surroundings (Ambrosi et al., 2011). For example, heart muscle can grow and remodel in response to changes in blood pressure (Rausch et al., 2011). Third, both the material microstructure and adaptive response influence mechanical behavior on multiple scales (Ambrosi et al., 2016). Therefore, even when a phenomena is well understood on one scale, it is not necessarily clear how that behavior will link across scales or how mechanical information will traverse scales and trigger adaptation (Lejeune et al., 2019). The inherently interesting nature of these challenges combined with the potential benefits of understanding, predicting, and ultimately controlling the mechanical behavior of biological materials has motivated researchers to develop novel numerical methods, and extend modeling frameworks originally formulated for engineered materials (Rodriguez et al., 1994).

Peridynamics, a theoretical and computational framework that is designed to unify the mechanics of discrete and continuous media, is a technique originally developed for fracture mechanics applications (Silling and Lehoucq, 2010). Rather than using partial differential equations to formulate the equations of motion, peridynamics uses integral equations which exist on crack surfaces (Silling, 2000; Silling et al., 2007). The first paper introducing peridynamics was published in 2000 and presents peridynamics as a methodology for modeling discontinuities and long range forces using a constitutive relation based on bond-based (i.e., pair-wise) interactions between particles (Silling, 2000). Since this original work, peridynamic theory has been developed numerically (Bobaru and Ha, 2011), extended to include more complex constitutive models (Silling et al., 2007; Warren et al., 2009), and applied to model a variety of engineered systems (Kilic and Madenci, 2010b). In the context of biological materials, peridynamics is a compelling method for capturing material fracture, for example, bone fracture (Deng et al., 2008; Ghajari et al., 2014), and for capturing material behavior where long-range forces are important, for example, in lipid membranes (Madenci et al., 2020). And, because the peridynamic framework deals comfortably with both continuous and discrete media, it is a compelling method for modeling biological tissue on the cell population scale where the material is, in reality, somewhere in-between (Lejeune and Linder, 2017a).

Over the course of the past decade, peridynamics has gained traction as a method for modeling biological materials. The range of this recent research is shown in Fig. 12.1. Peridynamics has been used to model diverse phenomena ranging from fracture to aspects of growth and remodeling (Javili et al., 2019). In this chapter, we will discuss some of these recent advances with an emphasis on adapting the peridynamic framework to capture mechanical behavior on the cell population scale. We begin in Section 2 with a brief methodological background; we highlight some notable applications in Section 3, and then we conclude in Section 4. We anticipate that in the coming decade the flexible nature of the peridynamics framework will lead to further adoption in modeling biological materials.

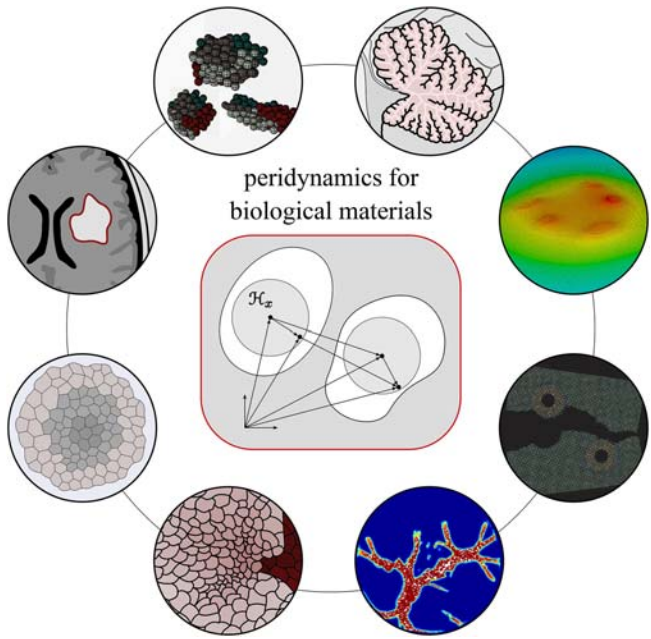

FIGURE 12.1 Examples adapted from the literature of models of biological materials based on peridynamics. Clockwise from the upper left: agent-based cell modeling (Lejeune et al., 2019), understanding emergent behavior in the cerebellum (Lejeune et al., 2019), modeling inclusions in lipid membranes (Madenci et al., 2020), modeling cortical bone fracture (Deng et al., 2008), modeling rupture in lipid membranes (Taylor et al., 2016), modeling tumor growth (Lejeune and Linder, 2017a), modeling mechanical inhomogeneities in growing spheroids (Lejeune and Linder, 2018a), and modeling tumor shrinkage (Lejeune and Linder, 2020).

2. Methodology

Here, we cover basic methodological advances for modeling biological materials with peridynamics. First, in Section 2.1, we briefly review the fundamental equations of peridynamics. Then, in Section 2.2, with a consistent notation, we introduce extensions to the framework that enable modeling biological mechanisms such as cell growth, division, and death, and present the fundamental equations in their corresponding discrete form. Finally, in Section 2.3, we cover the concept of emergent behavior in biological systems and provide additional context for understanding the results demonstrated in Section 3.

2.1 Background and notation

As stated in Section 1, peridynamics is a theoretical and computational framework where the classical balance equations are integrals rather than partial differential equations (Silling, 2000). Here we introduce the basic notation and equations, with key terms illustrated in Fig. 12.2. First, we introduce the concept of a horizon. In the peridynamic formulation, a given point $\boldsymbol{x}$ interacts with other points within its horizon $\mathcal{H}_{\boldsymbol{x}}$ where $\mathcal{H}_{\boldsymbol{x}}$ is a line (1D), circle (2D), or sphere (3D) defined by horizon size $\delta_{\boldsymbol{x}}$ and written as

$$\mathcal{H}_{\boldsymbol{x}} = \{\boldsymbol{x}' \mid \|\boldsymbol{x}' - \boldsymbol{x}\| < \delta_{\boldsymbol{x}}\}. \tag{12.1}$$

Physically, $\mathcal{H}_{\boldsymbol{x}}$ is defined as the domain where any particle will experience force exerted by $\boldsymbol{x}$. The two-dimensional case is illustrated in Fig. 12.2. In addition to the horizon, we introduce the dual-horizon, which will allow for nonuniformity in horizon size across different points (Ren et al., 2016), specifically the case where some point $\boldsymbol{x}$ is within the horizon of $\boldsymbol{x}'$ but $\boldsymbol{x}'$ is not within the horizon of $\boldsymbol{x}$ (Bobaru et al., 2009; Bobaru and Ha, 2011). The dual horizon is defined as the union of points whose horizons include $\boldsymbol{x}$, written as

$$\mathcal{H}'_{\boldsymbol{x}} = \{\boldsymbol{x}' \mid \boldsymbol{x} \in \mathcal{H}_{\boldsymbol{x}'}\}. \tag{12.2}$$

For all points $\boldsymbol{x}$ within $\mathcal{H}_{\boldsymbol{x}'}$, $\boldsymbol{x}'$ acts on $\boldsymbol{x}$. And, unlike the horizon, the dual horizon is not necessarily a circle or sphere. However, if the horizon size $\delta_{\boldsymbol{x}}$ does not vary across points, then $\mathcal{H}_{\boldsymbol{x}} = \mathcal{H}'_{\boldsymbol{x}}$ and the dual-horizon formulation will be identical to that of conventional peridynamics.

The equation of motion is formulated as an integral of interaction forces between points on the body Ω. Here we introduce the terminology required to define the balance of linear momentum. Material points in the initial configuration Ω_0 are illustrated in Fig. 12.2A as $\boldsymbol{x}$ and $\boldsymbol{x}'$. The bond vector between $\boldsymbol{x}$ and $\boldsymbol{x}'$ in the initial configuration is defined by the term

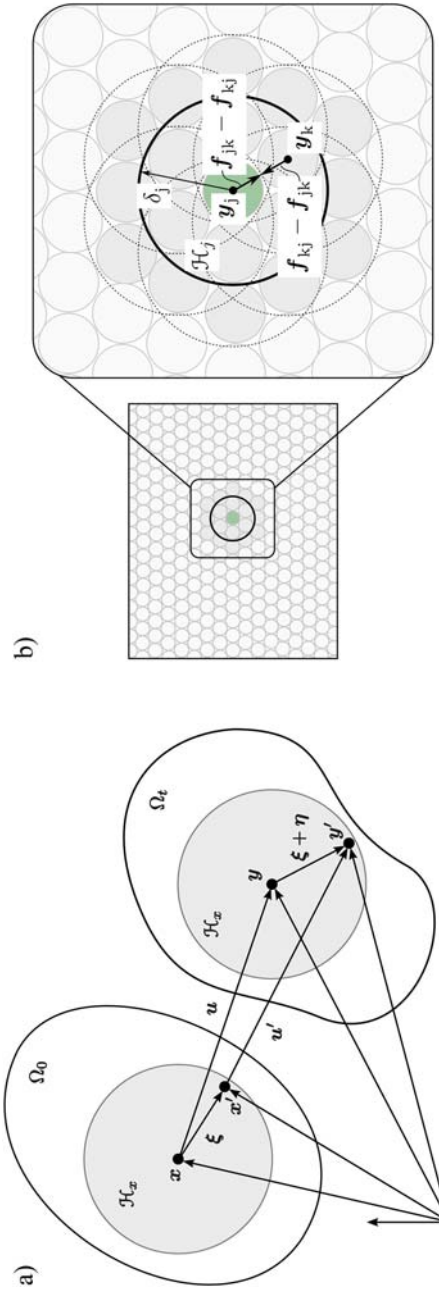

FIGURE 12.2 Illustration of key notation: (A) illustration of the reference configuration mapped to the deformed configuration; (B) illustration of model implementation in the mesh-free setting.

$\boldsymbol{\xi} = \boldsymbol{x}' - \boldsymbol{x}$. In the discrete setting, and in numerical implementation, point $\boldsymbol{x}$ is referred to as node j, point $\boldsymbol{x}'$ is referred to as node k, and the bond between them is defined as $\boldsymbol{\xi}_{jk} = \boldsymbol{x}_k - \boldsymbol{x}_j$. The displacement vector $\boldsymbol{u}(\boldsymbol{x}, t)$ and position vector $\boldsymbol{y}(\boldsymbol{x}, t) = \boldsymbol{x} + \boldsymbol{u}(\boldsymbol{x}, t)$, illustrated in Fig. 12.2A, are defined in the current configuration. The relative displacement of a bond is then defined as $\boldsymbol{\eta} = \boldsymbol{u}' - \boldsymbol{u}$, and described in the discrete setting as $\boldsymbol{\eta}_{\mathrm{jk}} = \boldsymbol{u}_{\mathrm{k}} - \boldsymbol{u}_{\mathrm{j}}$. Here we adopt the typical state notation where we define a state of order m as a function $\underline{\boldsymbol{A}}\langle \bullet \rangle$ that maps the vector in angle brackets $\langle \bullet \rangle$ to a tensor of order m (Silling et al., 2007). For example, the relative position of bond $\boldsymbol{\xi}$ can be written as $\underline{\boldsymbol{y}}\langle \boldsymbol{\xi} \rangle = \boldsymbol{y}(\boldsymbol{x}', t) - \boldsymbol{y}(\boldsymbol{x}, t) = \boldsymbol{\xi} + \boldsymbol{\eta}$. In this chapter, states are written with an underline, and angle brackets are used to indicate the quantity which the state function is acting on.

In dual-horizon peridynamics, the force between points $\boldsymbol{x}$ and $\boldsymbol{x}'$ is defined in two distinct steps, first using the dual horizon and then using the horizon. We define force density vector $\boldsymbol{f}_{\boldsymbol{x}\boldsymbol{x}'}(\boldsymbol{\eta}, \boldsymbol{\xi})$ as the force per volume acting on particle $\boldsymbol{x}$ due to particle $\boldsymbol{x}'$. Point $\boldsymbol{x}$ is the location of the force and $\boldsymbol{x}'$ is the source of the force. Likewise, $\boldsymbol{f}_{\boldsymbol{x}'\boldsymbol{x}}(-\boldsymbol{\eta}, -\boldsymbol{\xi})$ is the force density vector acting on particle $\boldsymbol{x}'$ due to particle $\boldsymbol{x}$. Each force density, $\boldsymbol{f}_{\boldsymbol{x}\boldsymbol{x}'}$ acting on $\boldsymbol{x}$, is then accompanied by a reaction force density, $-\boldsymbol{f}_{\boldsymbol{x}\boldsymbol{x}'}$ acting on $\boldsymbol{x}'$. The direct force density at $\boldsymbol{x}$ is computed from points in the dual horizon of $\boldsymbol{x}$ and the reaction force density at $\boldsymbol{x}$ is computed from points in the horizon of $\boldsymbol{x}$. Therefore, the net force density acting on point $\boldsymbol{x}$ due to bond $\boldsymbol{x}$–$\boldsymbol{x}'$ is a sum of the direct force density and reaction force density written as

$$\boldsymbol{f}_{\boldsymbol{x}\boldsymbol{x}'}(\boldsymbol{\eta}, \boldsymbol{\xi}) - \boldsymbol{f}_{\boldsymbol{x}'\boldsymbol{x}}(-\boldsymbol{\eta}, -\boldsymbol{\xi}). \tag{12.3}$$

And, the net force density acting on a point $\boldsymbol{x}'$ due to bond $\boldsymbol{x}$–$\boldsymbol{x}'$ is

$$\boldsymbol{f}_{\boldsymbol{x}'\boldsymbol{x}}(-\boldsymbol{\eta}, -\boldsymbol{\xi}) - \boldsymbol{f}_{\boldsymbol{x}\boldsymbol{x}'}(\boldsymbol{\eta}, \boldsymbol{\xi}). \tag{12.4}$$

By accounting for the contributions from $\mathcal{H}_{\boldsymbol{x}}'$ and $\mathcal{H}_{\boldsymbol{x}}$ (and subsequently direct and reaction forces) separately, the antisymmetry of net force density is preserved in the case of variable horizon size.

Given the kinematic description and definition of force density, we can define the balance of linear momentum (Silling, 2000). The inertial force, body force, and internal force terms at point $\boldsymbol{x}$ and time t are equated as

$$\rho \ddot{\boldsymbol{u}}(\boldsymbol{x}, t) = \int_{\boldsymbol{x}' \in \mathcal{H}_{\boldsymbol{x}}'} \boldsymbol{f}_{\boldsymbol{x}\boldsymbol{x}'}(\boldsymbol{\eta}, \boldsymbol{\xi}) \mathrm{d}V_{\boldsymbol{x}'} - \int_{\boldsymbol{x}' \in \mathcal{H}_{\boldsymbol{x}}} \boldsymbol{f}_{\boldsymbol{x}'\boldsymbol{x}}(-\boldsymbol{\eta}, -\boldsymbol{\xi}) \mathrm{d}V_{\boldsymbol{x}'} + \boldsymbol{b}(\boldsymbol{x}, t) \tag{12.5}$$

where ρ is density, $\ddot{\boldsymbol{u}}$ is acceleration, and $\boldsymbol{b}$ is body force (Ren et al., 2016). Integrating over the dual horizon $\mathcal{H}_{\boldsymbol{x}}'$ contributes the direct force term acting on point $\boldsymbol{x}$, and integrating over the horizon $\mathcal{H}_{\boldsymbol{x}}$ contributes the reaction

force term. The discrete form of the balance of linear momentum is then written as

$$\rho\ddot{\boldsymbol{u}}(\boldsymbol{x}_\mathrm{j},t)=\sum_{\mathrm{k}\in\mathcal{H}_\mathrm{j}'}\boldsymbol{f}_\mathrm{jk}(\boldsymbol{\eta}_\mathrm{jk},\boldsymbol{\xi}_\mathrm{jk})\Delta V_\mathrm{k}-\sum_{\mathrm{k}\in\mathcal{H}_\mathrm{j}}\boldsymbol{f}_\mathrm{kj}(-\boldsymbol{\eta}_\mathrm{jk},-\boldsymbol{\xi}_\mathrm{jk})\Delta V_\mathrm{k}+\boldsymbol{b}(\boldsymbol{x}_\mathrm{j},t) \tag{12.6}$$

where the integral in Eq. (12.5) is simply replaced by a summation. We note that in the numerical implementation of dual-horizon peridynamics it is not necessary to compute the dual horizon explicitly. This equation can be assembled by looping through the horizon of each node and subsequently inferring each node's dual horizon (Ren et al., 2016).

Next, we define the equation for force density $\boldsymbol{f}_{\boldsymbol{x}\boldsymbol{x}'}$ with a constitutive law based on ordinary state-based peridynamics (Silling et al., 2007). The qualification "state-based" comes from the state notation defined previously. In state-based peridynamics, bond force is a function of the *collective* deformation of all bonds that act on the same points as the bond in question. Peridynamics is a nonlocal theory meaning that nonadjacent points can interact. The degree to which nonlocal forces come into play is controlled by two parameters: the horizon size δ and the influence function $\underline{\omega}\langle\boldsymbol{\xi}\rangle$. The influence function can be chosen to weight the effect of certain bonds more heavily or it can be set to a constant. For example, $\underline{\omega}\langle\boldsymbol{\xi}\rangle$ can be equal to

$$\underline{\omega}\langle\boldsymbol{\xi}\rangle=\exp\left(-\frac{\|\boldsymbol{\xi}\|^2}{\delta^2}\right)\quad\text{or}\quad\underline{\omega}\langle\boldsymbol{\xi}\rangle=1 \tag{12.7}$$

or another appropriate function (Ren et al., 2016; Littlewood, 2015). Given a chosen influence function, we can then compute the influence function weighted volume of the horizon at point $\boldsymbol{x}$, $m_{\boldsymbol{x}}$, by integrating over $\mathcal{H}_{\boldsymbol{x}}$ as

$$m_{\boldsymbol{x}}=\int_{\mathcal{H}_x}\underline{\omega}\langle\boldsymbol{\xi}\rangle\boldsymbol{\xi}\cdot\boldsymbol{\xi}\mathrm{d}V_\xi. \tag{12.8}$$

In addition, we define extension state $\underline{e}\langle\boldsymbol{\xi}\rangle$ as

$$\underline{e}\langle\boldsymbol{\xi}\rangle=\|\boldsymbol{\xi}+\boldsymbol{\eta}\|-\|\boldsymbol{\xi}\| \tag{12.9}$$

based on the bonds deformation. Using $m_{\boldsymbol{x}}$ defined at point $\boldsymbol{x}$ and $\underline{e}\langle\boldsymbol{\xi}\rangle$ defined for each bond associated with $\boldsymbol{x}$, we then compute the dilation at $\boldsymbol{x}$:

$$\theta_{\boldsymbol{x}}=\frac{n}{m_{\boldsymbol{x}}}\int_{\mathcal{H}_x}\underline{\omega}\langle\boldsymbol{\xi}\rangle\|\boldsymbol{\xi}\|\underline{e}\langle\boldsymbol{\xi}\rangle\mathrm{d}V_\xi \tag{12.10}$$

where n is the dimension number, $n \in \{2, 3\}$. The deviatoric extension state for bond $\boldsymbol{\xi}$ from the perspective of point $\boldsymbol{x}$ is then computed as

$$\underline{e}^d\langle \boldsymbol{\xi} \rangle = \underline{e}\langle \boldsymbol{\xi} \rangle - \frac{\theta_{\boldsymbol{x}} ||\boldsymbol{\xi}||}{n}. \tag{12.11}$$

With these terms, the scalar force state that defines the linear elastic ordinary state-based constitutive law for each bond $\boldsymbol{\xi}$ from the perspective of point $\boldsymbol{x}$ is written as

$$\underline{t}_{\boldsymbol{x}'\boldsymbol{x}} = \frac{n\kappa\theta_{\boldsymbol{x}}}{m_{\boldsymbol{x}}} \underline{\omega}\langle \boldsymbol{\xi} \rangle ||\boldsymbol{\xi}|| + \frac{n(n+2)\mu}{m_{\boldsymbol{x}}} \underline{\omega}\langle \boldsymbol{\xi} \rangle \underline{e}^d\langle \boldsymbol{\xi} \rangle \tag{12.12}$$

where κ and μ are the Lamé parameters bulk modulus and shear modulus, respectively (Littlewood, 2015). Given the scalar force state $\underline{t}$, the force density vectors corresponding with each bond are computed as

$$\boldsymbol{f}_{\boldsymbol{x}'\boldsymbol{x}}(\boldsymbol{\eta}, \boldsymbol{\xi}) = \underline{t}_{\boldsymbol{x}'\boldsymbol{x}} \frac{-\boldsymbol{\eta} - \boldsymbol{\xi}}{||\boldsymbol{\eta} + \boldsymbol{\xi}||} \tag{12.13}$$

which is the action force applied at point $\boldsymbol{x}'$, and

$$-\boldsymbol{f}_{\boldsymbol{x}'\boldsymbol{x}}(\boldsymbol{\eta}, \boldsymbol{\xi}) = \underline{t}_{\boldsymbol{x}'\boldsymbol{x}} \frac{\boldsymbol{\eta} + \boldsymbol{\xi}}{||\boldsymbol{\eta} + \boldsymbol{\xi}||} \tag{12.14}$$

which is the reaction force applied at point $\boldsymbol{x}$. To compute the total force at each point, force density vectors are summed over all bonds in the horizon. For more detail, we direct the reader to the peridynamics literature (Littlewood, 2015; Madenci and Oterkus, 2014; Oterkus, 2015; Silling and Lehoucq, 2010).

2.2 Implementing growth and remodeling

Starting from the background given in Section 2.1, we now highlight one strategy for adding growth and remodeling to the peridynamic framework. Specifically, we discuss using peridynamics to model cellular behavior on the microscale. We note that a description of additional cases, for example, adding macroscale growth alone, can be found in the literature (Lejeune and Linder, 2017a). In this example, we treat each cell as an individual node and use the peridynamic equation of motion to maintain mechanical equilibrium (Lejeune and Linder, 2017a). With this treatment, it is possible to implement an algorithm, illustrated in Fig. 12.3, where the peridynamic framework interacts with a biological algorithm and is used to maintain mechanical equilibrium in a defined system (Lejeune and Linder, 2017a). Essentially, after each simulation step of algorithmically defined cell behavior, the entire system is relaxed back to mechanical equilibrium via an adaptive dynamic relaxation procedure (Kilic and

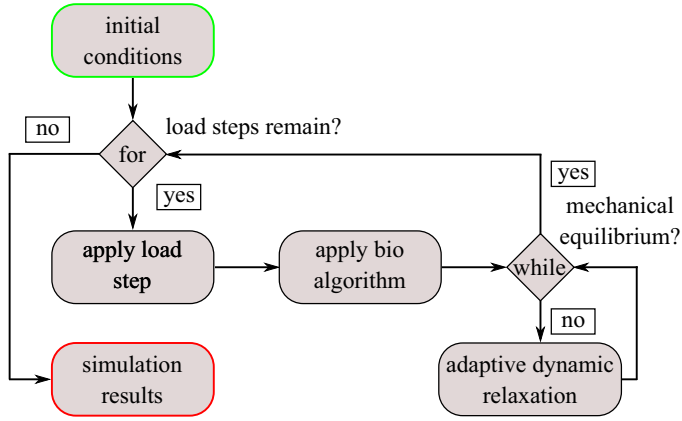

FIGURE 12.3 An example of an algorithm where a biological mechanism such as cell death or cell division is implemented in conjunction with the peridynamic equation of motion.

Madenci, 2010a). Here we redefine the constitutive relations in a manner that makes this possible and introduce the equations from Section 2.1 in their discrete form. First, we redefine the stretch-free separation distance between nodes as

$$\left\|\boldsymbol{\xi}_{jk}\right\| = (1+g_j)r_j + (1+g_k)r_k \tag{12.15}$$

where r is the initial radius associated with each node (cell), and g is the radial growth (or shrinkage) associated with each node where $-1 < g < g_{max}$. Given $||\boldsymbol{\xi}_{jk}||$, we define the stretch between node j and node k as

$$s_{jk} = \frac{\left\|\boldsymbol{y}_k - \boldsymbol{y}_j\right\| - \left\|\boldsymbol{\xi}_{jk}\right\|}{\left\|\boldsymbol{\xi}_{jk}\right\|} \tag{12.16}$$

which is used to determine bond damage γ_{jk} following

$$\gamma_{jk} = \begin{cases} 1 & \text{if } s < s_{max} \\ 0 & \text{otherwise} \end{cases} \tag{12.17}$$

with s_{max} defined as the maximum allowable stretch between bonds. Depending on the application, bond damage can be either reversible or irreversible (Lejeune and Linder, 2017a). We then define influence function ω as simply

$$\omega_{jk} = \gamma_{jk}. \tag{12.18}$$

The discrete form of the horizon weighted volume m is written as

$$m_j = \sum_{k \in \mathcal{H}_j} \omega_{jk} \|\boldsymbol{\xi}_{jk}\|^2 \Delta V_k \tag{12.19}$$

where ΔV_{k} is a function of r and g, and bond elongation e is written as

$$e_{jk} = \|\boldsymbol{y}_k - \boldsymbol{y}_j\| - \|\boldsymbol{\xi}_{jk}\|. \tag{12.20}$$

The discrete form of dilation θ is written as

$$\theta_j = \frac{n}{m_j} \sum_{k \in \mathcal{H}_j} \omega_{jk} \|\boldsymbol{\xi}_{jk}\| e_{jk} \Delta V_k \tag{12.21}$$

and deviatoric bond elongation e^d is defined as

$$e^d_{jk} = e_{jk} - \frac{\theta_j \|\boldsymbol{\xi}_{jk}\|}{n} \tag{12.22}$$

where $n = 2$ for a two-dimensional problem and $n = 3$ for a three-dimensional problem. With these terms, the equation for the magnitude of force density that arises at node k due to node j is

$$t_{kj} = \frac{n\kappa\theta_j}{m_j} \omega_{jk} \|\boldsymbol{\xi}_{jk}\| + \frac{n(n+2)\mu}{m_j} \omega_{jk} e^d_{jk} \tag{12.23}$$

where κ and μ are Lamé parameters. Building on these definitions, force density is defined as

$$\begin{aligned} \boldsymbol{f}_{jk}(\boldsymbol{y}_j, \boldsymbol{y}_k) &= t_{jk} \cdot \frac{\boldsymbol{y}_k - \boldsymbol{y}_j}{\|\boldsymbol{y}_k - \boldsymbol{y}_j\|} \\ \boldsymbol{f}_{kj}(\boldsymbol{y}_j, \boldsymbol{y}_k) &= t_{kj} \cdot \frac{-(\boldsymbol{y}_k - \boldsymbol{y}_j)}{\|\boldsymbol{y}_k - \boldsymbol{y}_j\|} \end{aligned} \tag{12.24}$$

where only position in the current configuration $\boldsymbol{y}$ defines the direction of force density. In Table 12.1 we list standard ranges for the parameters required to implement these equations.

2.3 Note on emergent behavior

In computational modeling of biological materials, there is an inherent trade-off between continuous and discrete approaches. Continuum modeling is typically used to understanding materials on the macroscale, where biological materials are treated as either growing surfaces (Rudraraju et al., 2019), volumetrically growing solids (Javili et al., 2015), or as constituents in a mixture theory approach (Byrne, 2003; Preziosi and

TABLE 12.1 This table summarizes typical parameter ranges for agent-based cell simulations. We note that a framework for running a global sensitivity analysis on these and other parameters has been presented in the literature (Lejeune and Linder, 2018b, 2020).

Parameter	Value	Source
δ_0	$1.01 - 1.15$	Plausible values (Lejeune and Linder, 2017a)
s_{max}	$1.0 - 2.0$	Plausible values (Lejeune and Linder, 2017a)
E	1 kPa	Plausible value (Xu et al., 2012)
ν	0.45	Nearly incompressible material
r_0	5 μm	Approximate cell size (Drasdo and Hohme, 2005)

Tosin, 2008). Discrete modeling, on the other hand, views biological materials as a collection of cellular and/or subcellular components (Drasdo et al., 2007; Sandersius and Newman, 2008). Discrete modeling, which is often favored by the biophysics community (Norton et al., 2010), allows a mechanistic description of cell behavior, but is computationally intractable on the macroscale, which severely limits many potential applications in the clinical setting such as modeling the macroscale mechanical interactions between tumors and healthy tissue or organs (Frieboes et al., 2007; Lowengrub et al., 2010). To capture the benefits of both discrete and continuum modeling, hybrid modeling approaches have been proposed (Stolarska et al., 2009). For example, one approach treats active cells on the perimeter of a growing system as discrete particles and the inactive cells at the center of the system as a continuum captured by a finite element mesh (Kim et al., 2007). In addition, there has been significant effort to formulate continuum models that phenomenologically reflect cellular scale behavior (Ambrosi et al., 2012; Araujo and McElwain, 2004). And, more recently, researchers have explored multiscale modeling frameworks for biological materials (Khang et al., 2020).

In several of the results presented in Section 3, the goal is to understand how phenomena observed on the cellular scale will ultimately influence macroscale tissue behavior. Essentially, given some known cellular-scale mechanism such as cell division or cell death, what macroscale growth and remodeling-related behavior will *emerge*? Here we briefly define two

tools for summarizing the results of agent-based cell models that will allow us to quantify emergent behavior. First, we define the average growth-induced deformation gradient $\boldsymbol{F}$. Examples of this are illustrated in Figs. 12.4–12.6. To compute the average growth-induced deformation $\boldsymbol{F}$, we define an array of initial stretch vectors $\boldsymbol{\Lambda}_0$ as

$$\boldsymbol{\Lambda}_0 = \left[\lambda_{0_1}^1 \lambda_{0_1}^2 \ldots \lambda_{0_1}^{p_1} \lambda_{0_2}^1 \lambda_{0_2}^2 \ldots \lambda_{0_2}^{p_2} \ldots \lambda_{0_n}^1 \lambda_{0_n}^2 \ldots \lambda_{0_n}^{p_n}\right]. \tag{12.25}$$

Then, we define an array of current stretch vectors $\boldsymbol{\Lambda}_t$ which reflects the initial stretch vectors tracked into the current configuration:

$$\boldsymbol{\Lambda}_t = \left[\lambda_{t_1}^1 \lambda_{t_1}^2 \ldots \lambda_{t_1}^{p_1} \lambda_{t_2}^1 \lambda_{t_2}^2 \ldots \lambda_{t_2}^{p_2} \ldots \lambda_{t_n}^1 \lambda_{t_n}^2 \ldots \lambda_{t_n}^{p_n}\right] \tag{12.26}$$

where p reflects initial vector repeats due to cell splitting as illustrated in Fig. 12.5C. In the case of cell death, as in Fig. 12.6, only vectors that are present in both configurations are considered. Given these arrays, we then define average deformation in the current configuration $\boldsymbol{F}$ with the equation

$$\boldsymbol{F}\boldsymbol{\Lambda}_0 = \boldsymbol{\Lambda}_t. \tag{12.27}$$

To solve this over-determined system of equations, we use the normal equation $\boldsymbol{F} = \boldsymbol{\Lambda}_t \boldsymbol{\Lambda}_0^T \left(\boldsymbol{\Lambda}_0 \boldsymbol{\Lambda}_0^T\right)^{-1}$. We can also define change in volume with respect to deformation as $J = \det\ \mathbf{F}$.

In addition to summarizing average population deformation, we define average population connectivity C. To compute C, we treat the population of cells as a mathematical graph structure G (Newman, 2010). Each cell is treated as a node in graph G. For every cell pair (j, k) where the physical distance between node j and node k is less than or equal to $r_j + r_k$, there is a corresponding edge in G between nodes j and k. This is illustrated in Fig. 12.6C. Average population connectivity C is then defined as

$$C = \frac{N_G^{1/d}}{m_{SG}} \times \frac{N_{SG}}{N_G} \tag{12.28}$$

where N_G is the number of nodes in G, N_{SG} is the number of nodes in the largest connected subgroup, $d = 2$ or $d = 3$ is the dimension of the problem, and m_{SG} is the dimensionless mean shortest path in the largest connected subgroup. The results in Section 3 show the ratio of connectivity at the end of the simulation to connectivity at the start of the simulation C_f/C_0. We note that both $\boldsymbol{F}$ and C have the added benefit of being a convenient way to summarize complicated model results with potential stochastic variation (Lejeune and Linder, 2020).

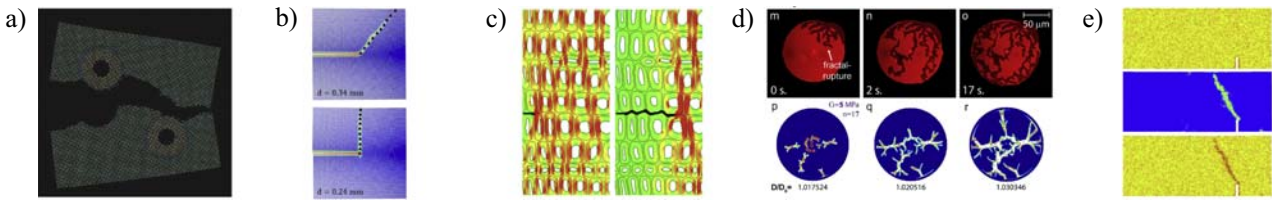

FIGURE 12.4 Examples from the literature relevant to modeling fracture in biological materials with peridynamics: (A) the relationship between fracture and healing in cortical bone (Deng et al., 2008); (B) fracture in anisotropic cortical bone (Ghajari et al., 2014); (C) fracture in wood (Perré et al., 2016); (D) rupture of biological membranes (Taylor et al., 2016); (E) fracture in a porous material (Chen et al., 2019). *All figures are adapted from the original manuscripts cited.*

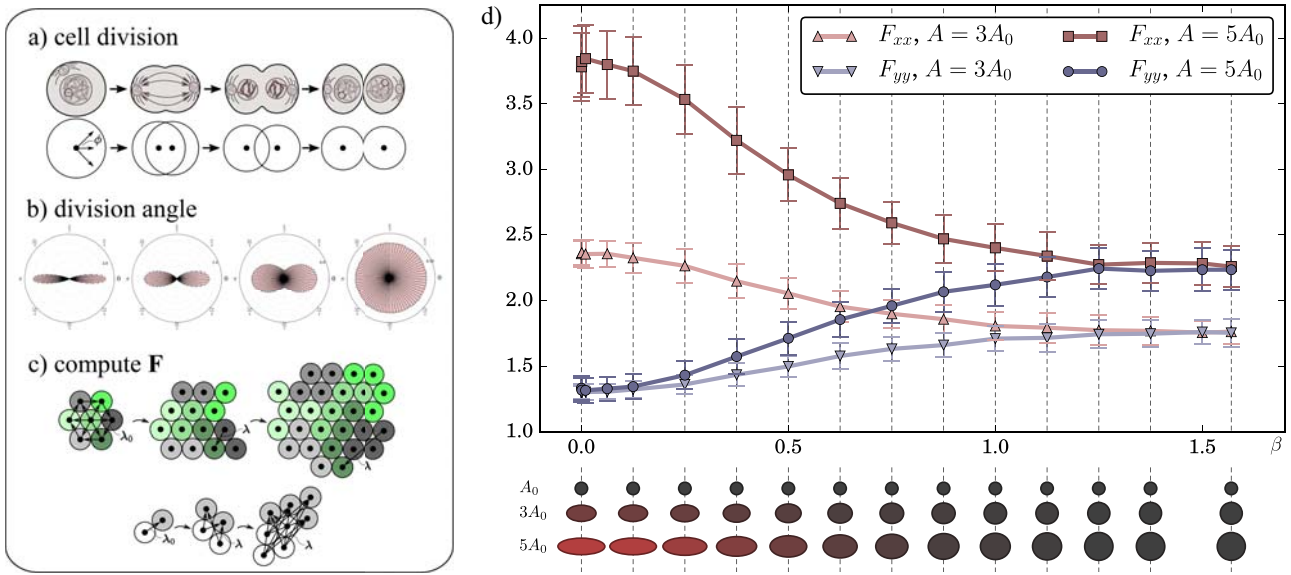

FIGURE 12.5 Investigating cell division–driven tissue growth with a peridynamics-based model: (A) illustration of cell division; (B) different probability density functions for cell division angle in 2D; (C) method for computing an approximate growth-induced deformation gradient from an agent-based cell model (see Section 2.3 for additional details); (D) components of the growth-induced deformation gradient as a function of underlying division angle distribution where $\varphi = \beta\mathcal{N}(0,1)$. *Information is adapted from Lejeune, E., Linder, C., 2017b. Quantifying the relationship between cell division angle and morphogenesis through computational modeling. J. Theor. Biol. 418, 1–7.*

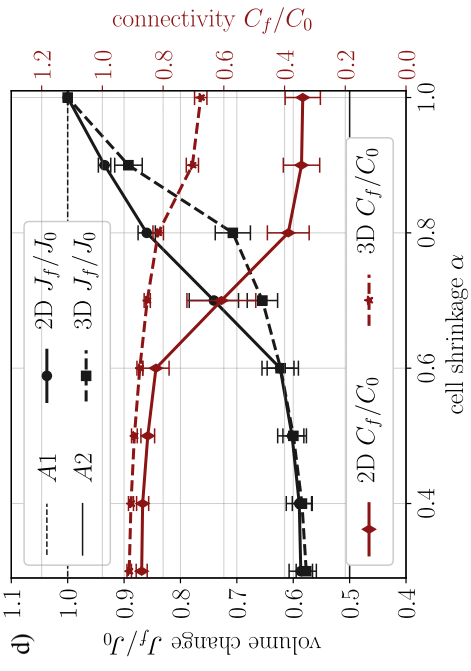

FIGURE 12.6 Investigating cell death–driven tissue shrinkage with a peridynamics-based model: (A) illustration of cell death; (B) method for computing an approximate growth-induced deformation gradient from an agent-based cell model; (C) method for computing cell population connectivity based on graph theory (see Section 2.3 for additional details); (D) components of the growth-induced displacement-based volume change and population connectivity as a function of cell shrinkage during death. *Information is adapted from Lejeune, E., Linder, C., 2020. Interpreting stochastic agent-based models of cell death. Comput. Methods Appl. Mech. Eng. 360, 112700.*

3. Example applications

In this section, we discuss three broad examples of peridynamics applied to modeling biological materials. First, in Section 3.1, we highlight several examples of fracture in biological materials. Then, in Section 3.2, we show how peridynamics can be used to better understand tissue growth and shrinkage. Finally, in Section 3.3, we show an example where peridynamic simulation is a part of a multiscale modeling framework designed to better understand mechanical contributions to cerebellar morphogenesis.

3.1 Fracture in biological materials

Peridynamics is best known as a method for modeling fracture (Madenci and Oterkus, 2014). Here we briefly note some examples of peridynamics being used to model fracture in biological materials. In Fig. 12.4A, we show an example of simulating fracture experiments in cortical bone (Deng et al., 2008). Notably, these simulations investigated the influence of weakened regions due to previous fracture and healing. Fig. 12.4B shows an example of simulating fracture experiments in cortical bone where the crack path depends on material anisotropy (Ghajari et al., 2014). We note that several recent advances in implementing anisotropic, porous, and spatially heterogeneous material behavior could potentially be relevant to simulating bone fracture (Karpenko et al., 2020). One such advance, simulating fracture in porous media, is shown in Fig. 12.4E (Chen et al., 2019). We also show an example of fracture in a complex wood microstructure in Fig. 12.4C (Perré et al., 2016), and rupture in a micron scale biological membrane in Fig. 12.4D (Taylor et al., 2016). Notably, there has been compelling recent work on simulating the complex behavior of inclusions in lipid membranes with peridynamics (Madenci et al., 2020). And, hyperelastic constitutive modeling, relevant to modeling soft tissue, has also been implemented in the peridynamic framework (Huang et al., 2019).

3.2 Tissue growth and shrinkage

Here we show two examples where peridynamics is used to better understand tissue growth and shrinkage. We note that in both cases, the peridynamic framework is used to model biological materials, populations of cells, that from a mechanics perspective are not strictly classified as either continuous or discrete.

3.2.1 Cell division and tissue growth

Significant effort has been made toward defining rules for predicting division angle in an individual cell (Gillies and Cabernard, 2011). And, external cues such as peptide gradients (Lamb et al., 2014), applied stretch (Wyatt et al., 2015), and applied force (Nestor-Bergmann et al., 2014) have all been shown to influence cell division angle. In studies of cell division orientation, division angle will vary even between tightly controlled experiments. Based on this experimentally observed variability, it follows that cell division angle is best understood as a random variable (Akanuma et al., 2016; Bosveld et al., 2016; Corrigan et al., 2015; Juschke et al., 2013). At present, it is unknown how the stochastic cell division angle influences morphogenesis on the population and tissue scales (Matamoroâ-Vidal et al., 2015; Minc and Piel, 2012).

To better understand how the distribution of division angle orientations will influence tissue scale growth, we implement a mechanics-based model of a population of cells where individual cells are represented with the peridynamic framework outlined in Section 2.2. We apply volumetric growth to each cell, and when cells exceed a threshold size they divide according to some probability distribution defined by angle φ, illustrated in Fig. 12.5B. The main quantitative simulation result is visualized in Fig. 12.5D, where the ellipses are visualizations of the average growth tensor, defined in Section 2.3, for a simulated cell population with respect to division angle probability distribution φ (Lejeune and Linder, 2017b). The peridynamic framework allows us to demonstrate that in certain systems the degree of anisotropy in population scale growth−induced deformation is directly connected to the underlying probability distribution of division angle φ.

3.2.2 Cell death and tissue shrinkage

The ability to robustly model cell death has important applications ranging from understanding anomalous organ development (Yamaguchi et al., 2011) to neurodegeneration (Weickenmeier et al., 2019). A particularly compelling example where an enhanced understanding of cell death on the organ scale would help guide clinical decision making is the case where tumors are located in a high stakes regions and can mechanically damage the surrounding tissue if they continue to grow, illustrated in Fig. 12.1 (Bellomo et al., 2008; Clatz et al., 2005; Deisboeck et al., 2011). In these cases, the relevant medical interventions such as radiation therapy and chemotherapy largely function by inducing cell death (Baskar et al., 2012; Cohen-Jonathan et al., 1999). Computational modeling is relevant because even when the response of individual cells to treatment is well understood, it is not necessarily straightforward how the cellular-scale

process of cell death will manifest on the macroscale. On the macroscale, many different fundamental modeling choices are potentially justifiable for capturing cell death. For example, macroscale tissue models may represent cell death as volumetric shrinkage, mechanical damage, a decrease in species concentration, or some combination of these mechanisms (Harris et al., 2018; Jain et al., 2014; Taber, 1995). The most applicable macroscale modeling choice will vary based on the specific type of cell death, illustrated in Fig. 12.6A (Majno and Joris, 1995), and the system in question (Ambrosi et al., 2016; Suzanne and Steller, 2013; Stylianopoulos, 2017).

With the peridynamic framework described in Section 2.2 and the analysis tools summarized in Section 2.3, we are able to take a bottom-up approach to show how differences in cell death on the cellular scale are linked to different interpretations of cell death on larger length scales. Specifically, we show that in some cases cell death leads to gaps between cells, while in other cases it lead to tissue shrinkage, illustrated in Fig. 12.6B and C. In Fig. 12.6D, we plot the change in population shrinkage J and average connectivity C, the two quantities of interest defined in Section 2.3 with respect to degree of radial cell shrinkage $\alpha = r_{\min}/r_0$ with all other parameters fixed. Clearly, the amount that a cell shrinks before it stops exerting force on its neighbors is important to population scale tissue behavior. When α is small (more shrinkage) cell death predominantly manifests as a volumetric change. When α is large, cell death predominantly manifests as a change in porosity and/or as an increase in material damage. Notably, Fig. 12.6D also shows that the results for both the two-dimensional and three-dimensional cases are quantitatively different. Unlike with a standard continuum model, the model based on peridynamics allows these differences to naturally emerge.

3.3 Connecting emergent behavior across scales

The cerebellum is a tightly folded structure located at the back of the head where the folds of the cerebellum are aligned such that the external surface appears to be covered in parallel grooves (Leto et al., 2015). Experiments have shown that a series of interconnected mechanisms drive cerebellar foliation (Sudarov and Joyner, 2007). However, the mechanism guiding the initial location of these folds, and subsequently cerebellar morphology, remains poorly understood (Leto et al., 2015). Critically, there is no definitive mechanistic explanation for the preferential emergence of parallel folds instead of the irregular folding pattern seen in the cerebral cortex (Lawton et al., 2019). With the framework defined in Sections 2.2 and 2.3, we are able to implement a multiscale model that connects the anisotropic cell division experimentally observed during cerebellar development (Legué et al., 2015) to anisotropic fold formation on the tissue scale (Lejeune et al., 2016). As shown in Fig. 12.7,

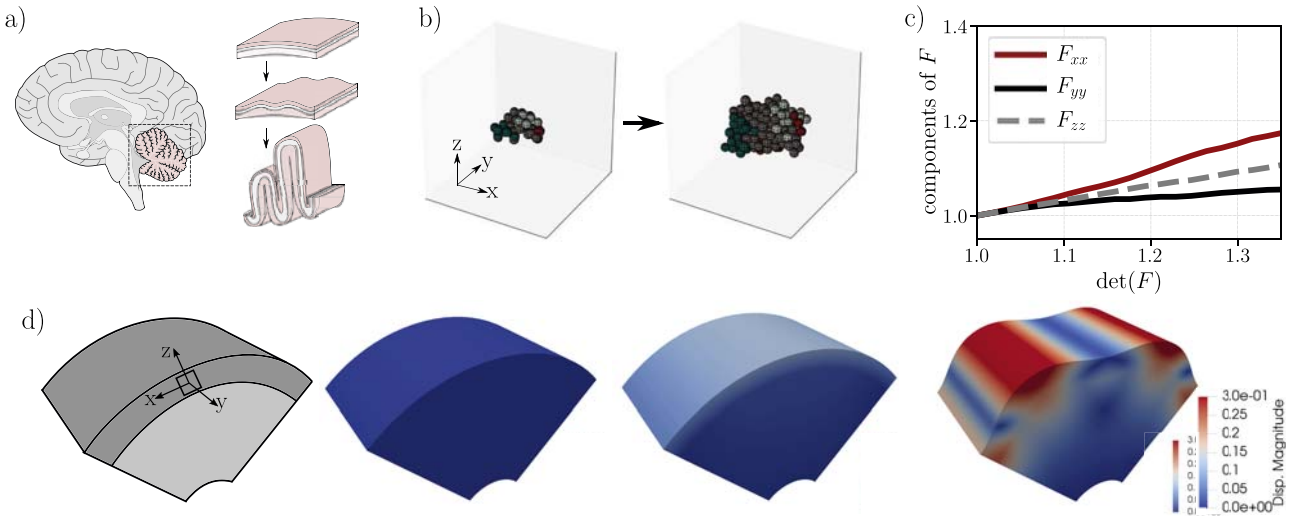

FIGURE 12.7 Investigating cerebellar morphogenesis with a peridynamics-based model: (A) illustration of cerebellar morphology and a schematic of cerebellar morphogenesis; (B) illustrated results of a single agent-based model simulation where the division angle is drawn from a probability distribution chosen to appear similar to the experimental results (Legué et al., 2015); (C) A plot of the components of $\boldsymbol{F}$ generated with the method described in Section 2.3; (D) The results of a tissue scale isogeometric analysis simulation where the growth-induced deformation gradient shown in (C) is applied to the outer layer of a cylindrically curved domain. *Information is adapted from Lejeune, E., Dortdivanlioglu, B., Kuhl, E., Linder, C., 2019. Understanding the mechanical link between oriented cell division and cerebellar morphogenesis. Soft Matter 15 (10), 2204–2215.*

we implement an agent-based model of simulated cell clones, propagate information from our in silico cell clones to a tissue-scale model, and use the framework to understand how differential growth between the cerebellar layers drives geometric instability in three-dimensional space. In the macroscale model, we study the influence of physically realistic anisotropic growth on surface wrinkling through both incremental stability analysis (Biot, 1965) and numerical modeling with isogeometric analysis (Hughes et al., 2005). By approaching this problem with fully three-dimensional models on both scales, we are able to better understand how the symmetry of the cerebellum emerges, rather than treating this symmetry as inherent and only presenting a model in two-dimensional space. Looking forward, the framework implemented here with a cellular-scale peridynamics-based model coupled to a macroscale continuum model is a powerful tool for understanding emergent behavior across scales.

4. Conclusion and outlook

In this chapter, we begin in Section 1 by introducing several reasons why modeling biological materials is a compelling research challenge. Then, we reviewed the basic equations for peridynamics in Section 2.1, described key details of adapting the peridynamic framework for biological materials in Section 2.2, and briefly describe methods for summarizing mechanically relevant results of agent-based model simulations in Section 2.3. In Section 3, we highlight three main applications for modeling biological materials with peridynamics: material fracture in Section 3.1, tissue growth and shrinkage in Section 3.2, and understanding emergent behavior across scales in Section 3.3. Practically, these applications cover bone fracture, lipid membrane rupture, tumor growth and shrinkage, and cerebellar morphogenesis.

Looking forward, we anticipate multiple avenues for future research in modeling biological materials with peridynamics. For example, there are numerous ways in which the peridynamic framework can be extended for modeling of biological systems ranging from implementing unique cell types and additional cellular-scale mechanisms to adding growth components to multiphysics constitutive laws. Furthermore, we anticipate that additional potential of the peridynamic framework could be realized through a class of models referred to as "hybrid models." In the broader literature of agent-based cell modeling, "hybrid models," where select locations contain discrete representations of cells and subcellular components while other locations are represented as a continuum, are gaining traction (Van Liedekerke et al., 2015, 2018). In particular, hybrid models

are being used to mitigate the prohibitive computational cost of implementing large agent-based models. Peridynamics, by nature, is a promising tool for hybrid modeling because it is specifically designed to unify the mechanics of continuous and discontinuous media. With the peridynamic framework, both "continuous" approximate regions and "discrete" highly resolved regions can be implemented with the same set of equations. Thus, the flexibility of the peridynamic framework could enable substantial further advances in computational modeling of biological materials beyond what we show here.

Acknowledgments

This work was supported by the National Science Foundation, United States of America Graduate Research Fellowship Grant No. DGE-114747 to EL and National Science Foundation, United States of America CAREER Grant No. CMMI-1553638 to CL.

References

Akanuma, T., Chen, C., Sato, T., Merks, R., Sato, T., 2016. Memory of cell shape biases stochastic fate decision-making despite mitotic rounding. Nat. Commun. 7.

Ambrosi, D., Ateshian, G., Arruda, E., Cowin, S., Dumais, J., Goriely, A., Holzapfel, G., Humphrey, J., Kemkemer, R., Kuhl, E., et al., 2011. Perspectives on biological growth and remodeling. J. Mech. Phys. Solid. 59 (4), 863–883.

Ambrosi, D., Preziosi, L., Vitale, G., 2012. The interplay between stress and growth in solid tumors. Mech. Res. Commun. 42, 87–91.

Ambrosi, D., Pezzuto, S., Riccobelli, D., Stylianopoulos, T., Ciarletta, P., 2016. Solid tumors are poroelastic solids with a chemo mechanical feedback on growth. J. Elasticity 1–18.

Araujo, R.P., McElwain, D.L.S., 2004. A linear-elastic model of anisotropic tumour growth. Eur. J. Appl. Math. 15 (3), 365–384. https://doi.org/10.1017/s0956792504005406.

Baskar, R., Lee, K., Yeo, R., Yeoh, K., 2012. Cancer and radiation therapy: current advances and future directions. Int. J. Med. Sci. 9 (3), 193.

Bellomo, N., Li, N.K., Maini, P.K., 2008. On the foundations of cancer modelling: selected topics, speculations, and perspectives. Math. Model Methods Appl. Sci. 18 (4), 593–646.

Biot, M.A., 1965. Mechanics of Incremental Deformations. John Wiley and Sons, New York.

Bobaru, F., Ha, Y.D., 2011. Adaptive refinement and multiscale modeling in 2d peridynamics. J. Multiscale Comput. Eng. 9 (6), 635–659.

Bobaru, F., Yang, M., Alves, L.F., Silling, S.A., Askari, E., Xu, J., 2009. Convergence, adaptive refinement, and scaling in 1d peridynamics. Int. J. Numer. Methods Eng. 77 (6), 852–877. https://doi.org/10.1002/nme.2439.

Bosveld, F., Markova, O., Guirao, B., Martin, C., Wang, Z., Pierre, A., Balakireva, M., Gaugue, I., Ainslie, A., Christophorou, N., Lubensky, D., 2016. Epithelial tricellular junctions act as interphase cell shape sensors to orient mitosis. Nature 530 (7591), 495.

Byrne, H., 2003. Modelling solid tumour growth using the theory of mixtures. Math. Med. Biol. 20 (4), 341–366. https://doi.org/10.1093/imammb/20.4.341.

Chen, Z., Niazi, S., Bobaru, F., 2019. A peridynamic model for brittle damage and fracture in porous materials. Int. J. Rock Mech. Min. Sci. 122, 104059.

Clatz, O., Sermesant, M., Bondiau, P.-Y., Delingette, H., Warfield, S.K., Malandain, G., Ayache, N., 2005. Realistic simulation of the 3-d growth of brain tumors in mr images

coupling diffusion with biomechanical deformation. IEEE Trans. Med. Imag. 24 (10), 1334–1346.
Cohen-Jonathan, E., Bernhard, E., McKenna, W., 1999. How does radiation kill cells? Curr. Opin. Chem. Biol. 3 (1), 77–83.
Corrigan, A., Shrestha, R., Draviam, V., Donald, A., 2015. Modeling of noisy spindle dynamics reveals separable contributions to achieving correct orientation. Biophys. J. 109 (7), 1398–1409.
Deisboeck, T.S., Wang, Z., Macklin, P., Cristini, V., 2011. Multiscale cancer modeling. Annu. Rev. Biomed. Eng. 13, 127–155.
Deng, Q., Chen, Y., Lee, J., 2008. An investigation of the microscopic mechanism of fracture and healing processes in cortical bone. Int. J. Damage Mech. 18 (5), 491–502. https://doi.org/10.1177/1056789508096563.
Drasdo, D., Hohme, S., 2005. A single cell based model of tumor growth in vitro monolayers and spheroids. Phys. Biol. 2 (3), 133–147.
Drasdo, D., Höhme, S., Block, M., 2007. On the role of physics in the growth and pattern formation of multi-cellular systems: what can we learn from individual-cell based models? J. Stat. Phys. 128 (1–2), 287–345.
Frieboes, H.B., Lowengrub, J.S., Wise, S., Zheng, X., Macklin, P., Bearer, E.L., Cristini, V., 2007. Computer simulation of glioma growth and morphology. Neuroimage 37, S59–S70. https://doi.org/10.1016/j.neuroimage.2007.03.008.
Ghajari, M., Iannucci, L., Curtis, P., 2014. A peridynamic material model for the analysis of dynamic crack propagation in orthotropic media. Comput. Methods Appl. Mech. Eng. 276, 431–452.
Gillies, T.E., Cabernard, C., 2011. Cell division orientation in animals. Curr. Biol. 21 (15), R599–R609.
Harris, T.C., de Rooij, R., Kuhl, E., 2018. The shrinking brain: cerebral atrophy following traumatic brain injury. Ann. Biomed. Eng. 1–19.
Huang, Y., Oterkus, S., Hou, H., Oterkus, E., Wei, Z., Zhang, S., 2019. Peridynamic model for visco-hyperelastic material deformation in different strain rates. Continuum Mech. Therm. 1–35.
Hughes, T.J.R., Cottrell, J.A., Bazilevs, Y., 2005. Isogeometric analysis: CAD, finite elements, NURBS, exact geometry and mesh refinement. Comput. Methods Appl. Mech. Eng. 194 (39–41), 4135–4195.
Jain, R., Martin, J., Stylianopoulos, T., 2014. The role of mechanical forces in tumor growth and therapy. Annu. Rev. Biomed. Eng. 16, 321–346.
Javili, A., Dortdivanlioglu, B., Kuhl, E., Linder, C., 2015. Computational aspects of growth-induced instabilities through eigenvalue analysis. Comput. Mech. 56 (3), 405–420.
Javili, A., Morasata, R., Oterkus, E., Oterkus, S., 2019. Peridynamics review. Math. Mech. Solids 24 (11), 3714–3739.
Juschke, C., Xie, Y., Postiglione, M.P., Knoblich, J.A., 2013. Analysis and modeling of mitotic spindle orientations in three dimensions. Proc. Natl. Acad. Sci. U S A 111 (3), 1014–1019.
Karpenko, O., Oterkus, S., Oterkus, E., 2020. Influence of different types of small-size defects on propagation of macro-cracks in brittle materials. J. Peridynamics Nonlocal Model. 2, 289–316. https://doi.org/10.1007/s42102-020-00032-z.
Khang, A., Howsmon, D.P., Lejeune, E., Sacks, M.S., 2020. Multi-scale modeling of the heart valve interstitial cell. In: Multi-scale Extracellular Matrix Mechanics and Mechanobiology. Springer, pp. 21–53.
Kilic, B., Madenci, E., 2010a. An adaptive dynamic relaxation method for quasi-static simulations using the peridynamic theory. Theor. Appl. Fract. Mech. 53 (3), 194–204.
Kilic, B., Madenci, E., 2010b. Peridynamic theory for thermomechanical analysis. IEEE Trans. Adv. Packag. 33 (1), 97–105.

Kim, Y., Stolarska, M.A., Othmer, H.G., 2007. A hybrid model for tumor spheroid growth in vitro I: theoretical development and early results. Math. Model Methods Appl. Sci. 1773–1798.

Lamb, B., Luo, W., Nagdas, S., Yousaf, M., 2014. Cell division orientation on biospecific peptide gradients. ACS Appl. Mater. Interfaces 6 (14), 11523–11528.

Lawton, A.K., Engstrom, T., Rohrbach, D., Omura, M., Turnbull, D.H., Mamou, J., Zhang, T., Schwarz, J.M., Joyner, A.L., 2019. Cerebellar folding is initiated by mechanical constraints on a fluid-like layer without a cellular pre-pattern. Elife 8, e45019. eLife Sciences Publications Limited.

Legué, E., Riedel, E., Joyner, A.L., 2015. Clonal analysis reveals granule cell behaviors and compartmentalization that determine the folded morphology of the cerebellum. Development 142, 1661–1671.

Lejeune, E., Linder, C., 2017a. Modeling tumor growth with peridynamics. Biomech. Model. Mechanobiol. 1–17.

Lejeune, E., Linder, C., 2017b. Quantifying the relationship between cell division angle and morphogenesis through computational modeling. J. Theor. Biol. 418, 1–7.

Lejeune, E., Linder, C., 2018a. Modeling mechanical inhomogeneities in small populations of proliferating monolayers and spheroids. Biomech. Model. Mechanobiol. 17 (3), 727–743.

Lejeune, E., Linder, C., 2018b. Understanding the relationship between cell death and tissue shrinkage via a stochastic agent-based model. J. Biomech. 73, 9–17.

Lejeune, E., Linder, C., 2020. Interpreting stochastic agent-based models of cell death. Comput. Methods Appl. Mech. Eng. 360, 112700.

Lejeune, E., Javili, A., Weickenmeier, E.J., Kuhl, C.L., 2016. Tri-layer wrinkling as a mechanism for anchoring center initiation in the developing cerebellum. Soft Matter 12, 5613–5620.

Lejeune, E., Dortdivanlioglu, B., Kuhl, E., Linder, C., 2019. Understanding the mechanical link between oriented cell division and cerebellar morphogenesis. Soft Matter 15 (10), 2204–2215.

Leto, K., Arancillo, M., Becker, E.B.E., Buffo, A., Chiang, C., Ding, B., Dobyns, W.B., Dusart, I., Haldipur, P., Hatten, M.E., Hoshino, M., Joyner, A.L., Kano, M., Kilpatrick, D.L., Koibuchi, N., Marino, S., Martinez, S., Millen, K.J., Millner, T.O., Miyata, T., Parmigiani, E., Schilling, K., Sekerková, G., Sillitoe, R.V., Sotelo, C., Uesaka, N., Wefers, A., Wingate, R.J.T., Hawkes, R., 2015. Consensus paper: cerebellar development. Cerebellum 15 (6), 789–828. https://doi.org/10.1007/s12311-015-0724-2. Online first.

Littlewood, D., 2015. Roadmap for Peridynamic Software Implementation. SAND Report, Sandia National Laboratories, Albuquerque, NM and Livermore, CA.

Lowengrub, J.S., Frieboes, H.B., Jin, F., Chuang, Y.-L., Li, X., Macklin, P., Wise, S.M., Cristini, V., 2010. Nonlinear modelling of cancer: bridging the gap between cells and tumours. Nonlinearity 23, R1–R91.

Madenci, E., Oterkus, E., 2014. Peridynamic Theory and its Applications. Springer.

Madenci, E., Barut, A., Purohit, P.K., 2020. A peridynamic approach to computation of elastic and entropic interactions of inclusions on a lipid membrane. J. Mech. Phys. Solid. 104046.

Majno, G., Joris, I., 1995. Apoptosis, oncosis, and necrosis. an overview of cell death. Am. J. Pathol. 146 (1), 3.

Matamoroâ-Vidal, A., Salazarâ-Ciudad, I., Houle, D., 2015. Making quantitative morphological variation from basic developmental processes: where are we? The case of the drosophila wing. Dev. Dynam. 244 (9), 1058–1073. https://anatomypubs.onlinelibrary.wiley.com/doi/full/10.1002/dvdy.24255.

Meador, W.D., Sugerman, G.P., Story, H.M., Seifert, A.W., Bersi, M.R., Tepole, A.B., Rausch, M.K., 2020. The regional-dependent biaxial behavior of young and aged mouse

skin: a detailed histomechanical characterization, residual strain analysis, and constitutive model. Acta Biomater. 101, 403–413.
Minc, N., Piel, M., 2012. Predicting division plane position and orientation. Trends Cell Biol. 22 (4), 193–200.
Nestor-Bergmann, A., Goddard, G., Woolner, S., 2014. Force and the spindle: mechanical cues in mitotic spindle orientation. Semin. Cell Dev. Biol. 34, 133–139.
Newman, M., 2010. Networks: An Introduction. Oxford university press.
Norton, K.-A., Wininger, M., Bhanot, G., Ganesan, S., Barnard, N., Shinbrot, T., 2010. A 2d mechanistic model of breast ductal carcinoma in situ (dcis) morphology and progression. J. Theor. Biol. 263 (4), 393–406. https://doi.org/10.1016/j.jtbi.2009.11.024.
Oterkus, S., 2015. Peridynamics for the Solution of Multiphysics Problems. Ph.D. thesis. The University of Arizona.
Perré, P., Almeida, G., Ayouz, M., Frank, X., 2016. New modelling approaches to predict wood properties from its cellular structure: image-based representation and meshless methods. Ann. For. Sci. 73 (1), 147–162.
Preziosi, L., Tosin, A., 2008. Multiphase modelling of tumour growth and extracellular matrix interaction: mathematical tools and applications. J. Math. Biol. 58 (4), 625–656.
Rausch, M., Dam, A., Göktepe, S., Abilez, O., Kuhl, E., 2011. Computational modeling of growth: systemic and pulmonary hypertension in the heart. Biomech. Model. Mechanobiol. 10 (6), 799–811.
Ren, H., Zhuang, X., Cai, Y., Rabczuk, T., 2016. Dual-horizon peridynamics. Int. J. Numer. Methods Eng. 108 (12), 1451–1476.
Rodriguez, E., Hoger, A., McCulloch, A., 1994. Stress-dependent finite growth in soft elastic tissue. J. Biomech. 27 (4), 455–467.
Rudraraju, S., Moulton, D.E., Chirat, R., Goriely, A., Garikipati, K., 2019. A computational framework for the morpho-elastic development of molluskan shells by surface and volume growth. PLoS Comput. Biol. 15 (7) e1007213.
Sandersius, S., Newman, T., 2008. Modeling cell rheology with the subcellular element model. Phys. Biol. 5 (1), 015002.
Shao, Y., Zhao, H.-P., Feng, X.-Q., Gao, H., 2012. Discontinuous crack-bridging model for fracture toughness analysis of nacre. J. Mech. Phys. Solid. 60 (8), 1400–1419.
Silling, S.A., Lehoucq, R.B., 2010. Peridynamic theory of solid mechanics. Adv. Appl. Mech. 44, 73–168.
Silling, S.A., Epton, M., Weckner, O., Xu, J., Askari, E., 2007. Peridynamic states and constitutive modeling. J. Elasticity 88 (2), 151–184.
Silling, S.A., 2000. Reformulation of elasticity theory for discontinuities and long-range forces. J. Mech. Phys. Solid. 48, 175–209.
Stolarska, M.A., Kim, Y., Othmer, H.G., 2009. Multi-scale models of cell and tissue dynamics. Phil. Trans. Math. Phys. Eng. Sci. 367 (1902), 3525–3553. https://doi.org/10.1098/rsta.2009.0095.
Stylianopoulos, T., 2017. The solid mechanics of cancer and strategies for improved therapy. J. Biomech. Eng. 139 (2), 021004.
Sudarov, A., Joyner, A.L., 2007. Cerebellum morphogenesis: the foliation pattern is orchestrated by multi-cellular anchoring centers. Neural Dev. 2 (December), 26.
Suzanne, M., Steller, H., 2013. Shaping organisms with apoptosis. Cell Death Differ. 20 (5), 669.
Taber, L., 1995. Biomechanics of growth, remodeling, and morphogenesis. Appl. Mech. Rev. 48 (8), 487–545.
Taylor, M., Gözen, I., Patel, S., Jesorka, A., Bertoldi, K., 2016. Peridynamic modeling of ruptures in biomembranes. PloS One 11 (11) e0165947.

Van Liedekerke, P., Palm, M., Jagiella, N., Drasdo, D., 2015. Simulating tissue mechanics with agent-based models: concepts, perspectives and some novel results. Comput. Part. Mech. 2 (4), 401–444.

Van Liedekerke, P., Buttenschön, A., Drasdo, D., 2018. Off-lattice agent-based models for cell and tumor growth: numerical methods implementation, and applications. In: In Numerical Methods and Advanced Simulation in Biomechanics and Biological Processes. Elsevier, pp. 245–267.

Warren, T.L., Silling, S.A., Askari, A., Weckner, O., Epton, M.A., Xu, J., 2009. A non-ordinary state-based peridynamic method to model solid material deformation and fracture. Int. J. Solid Struct. 46 (5), 1186–1195. https://doi.org/10.1016/j.ijsolstr.2008.10.029.

Weickenmeier, J., Jucker, M., Goriely, A., Kuhl, E., 2019. A physics-based model explains the prion-like features of neurodegeneration in Alzheimer's disease, Parkinson's disease, and amyotrophic lateral sclerosis. J. Mech. Phys. Solid. 124, 264–281.

Wyatt, T., Harris, A., Lam, M., Cheng, Q., Bellis, J., Dimitracopoulos, A., Kabla, A., Charras, G., Baum, B., 2015. Emergence of homeostatic epithelial packing and stress dissipation through divisions oriented along the long cell axis. Proc. Natl. Acad. Sci. U S A 112 (18), 5726–5731.

Xu, W., Mezencev, R., Kim, B., Wang, L., McDonald, J., Sulchek, T., 2012. Cell stiffness is a biomarker of the metastatic potential of ovarian cancer cells. PloS One 7 (10) e46609.

Yamaguchi, Y., Shinotsuka, N., Nonomura, K., Takemoto, K., Kuida, K., Yosida, H., Miura, M., 2011. Live imaging of apoptosis in a novel transgenic mouse highlights its role in neural tube closure. J. Cell Biol. 195 (6), 1047–1060.